

# Biomimetic Nucleation of Hydroxyapatite Crystals Mediated by *Antheraea pernyi* Silk Sericin Promotes Osteogenic Differentiation of Human Bone Marrow Derived Mesenchymal Stem Cells

Mingying Yang,<sup>\*,†,‡</sup> Yajun Shuai,<sup>†,‡</sup> Can Zhang,<sup>†,§</sup> Yuyin Chen,<sup>‡</sup> Liangjun Zhu,<sup>‡</sup> Chuanbin Mao,<sup>\*,||</sup> and Hongwei OuYang<sup>§</sup>

<sup>†</sup>Institute of Applied Bioresource Research, College of Animal Science, Zhejiang University, Yuhangtang Road 866, Hangzhou, 310058, China

<sup>§</sup>Center for Stem Cell and Tissue Engineering, School of Medicine, Zhejiang University, Hangzhou, China

<sup>||</sup>Department of Chemistry and Biochemistry, Stephenson Life Sciences Research Center, University of Oklahoma, 101 Stephenson Parkway, Norman, Oklahoma 73019-5300, United States

## S Supporting Information



**ABSTRACT:** Biomacromolecules have been used as templates to grow hydroxyapatite crystals (HAs) by biomimetic mineralization to fabricate mineralized materials for potential application in bone tissue engineering. Silk sericin is a protein with features desirable as a biomaterial, such as increased hydrophilicity and biodegradation. Mineralization of the silk sericin from *Antheraea pernyi* (*A. pernyi*) silkworm has rarely been reported. Here, for the first time, nucleation of HAs on *A. pernyi* silk sericin (AS) was attempted through a wet precipitation method and consequently the cell viability and osteogenic differentiation of BMSCs on mineralized AS were investigated. It was found that AS mediated the nucleation of HAs in the form of nanoneedles while self-assembling into  $\beta$ -sheet conformation, leading to the formation of a biomimeticized protein-based biomaterial. The cell viability assay of BMSCs showed that the mineralization of AS stimulated cell adhesion and proliferation, showing that the resultant AS biomaterial is biocompatible. The differentiation assay confirmed that the mineralized AS significantly promoted the osteogenic differentiation of BMSCs when compared to nonmineralized AS as well as other types of sericin (*B. mori* sericin), suggesting that the resultant mineralized AS biomaterial has potential in promoting bone formation. This result represented the first work proving the osteogenic differentiation of BMSCs directed by silk sericin. Therefore, the biomimetic mineralization of *A. pernyi* silk sericin coupled with seeding BMSCs on the resultant mineralized biomaterials is a useful strategy to develop the potential application of this unexplored silk sericin in the field of bone tissue engineering. This study lays the foundation for the use of *A. pernyi* silk sericin as a potential scaffold for tissue engineering.

## 1. INTRODUCTION

Bone is formed by a series of complex events involving mineralization with calcium phosphate in the form of hydroxyapatite crystals (HAs) on extracellular matrix.<sup>1–3</sup> Therefore, as a biomimetic strategy, many macromolecular materials have been used as templates to grow HAs to form mineralized materials that can be used as a building block for bone implant fabrication, such as collagen, phage, and silk fibroin.<sup>4–10</sup> HAs-coated silk fibroin promotes osteogenic differentiation of BMSCs,<sup>11,12</sup> which provides an appropriate osteoconductive environment for BMSCs to regenerate sufficient new bone tissue.<sup>13</sup> However, unlike silk fibroin, another silk-derived protein, silk sericin, has not been studied regarding how its HAs mineralization can affect the osteogenic differentiation of BMSCs.

Silk sericin is a global protein synthesized in the middle silk gland of silkworm, which is coated on the fibroin fiber when silkworm spins cocoon. In comparison to silk fibroin, silk sericin has its unique characteristics including hydrophilicity, oxidation resistance, ultraviolet resistance, and biodegradation.<sup>14–18</sup> The silk sericin from *Bombyx mori* (*B. mori*) silkworm, a well-known domesticated silkworm, can be mineralized, leading to improvement of the cell viability.<sup>19,20</sup> Thus, HAs-coated *B. mori* sericin (BS) has been proposed to form potential scaffolds for bone tissue engineering. Meanwhile, another silk sericin can be produced by *Antheraea pernyi* (*A. pernyi*) silkworm, a large species of wild silkworm, in large

Received: November 27, 2013

Revised: March 13, 2014

Published: March 26, 2014

quantity. The amino acid composition of *A. pernyi* sericin (AS) is different from that of BS with AS having a lower percentage of serine and tyrosine (Table S1). However, there is no report on the mineralization of AS and its potential application as a building block to build bone implants and scaffolds for bone tissue engineering. Therefore, the mineralization of AS needs to be investigated to fill this gap.

Hence, this study aimed to investigate AS-mediated nucleation of HAp to form mineralized AS and the impact of mineralization of AS on the osteogenic differentiation of BMSCs. Figure 1 shows our strategy to achieve this goal. We

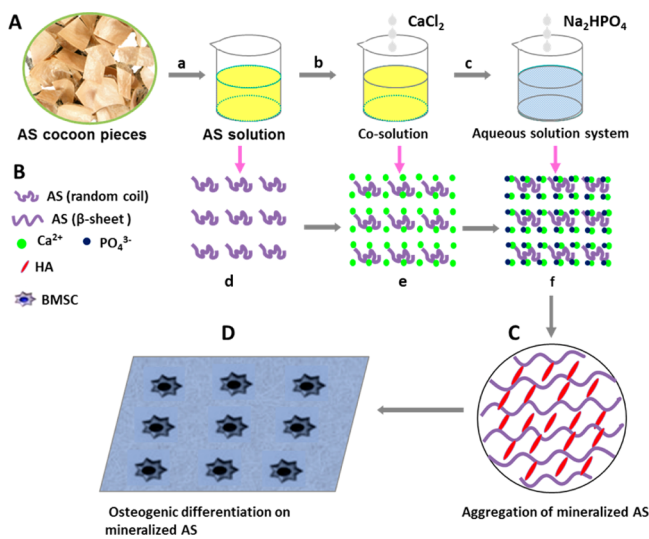


**Figure 1.** Mineralization of AS and its biological properties. (A) Schematic representing preparation of AS solution and its biominerilization; (B) Proposed schematic describing the nucleation of HAp mediated by AS; (C) The assembly structure of mineralized AS with  $\beta$ -sheet conformation; (D) The osteogenic differentiation of BMSCs on mineralized AS; (a) *A. pernyi* cocoons were heated in deionized water at 120 °C for 30 min and the AS solution was extracted; (b)  $\text{CaCl}_2$  solution was first added into AS solution; (c)  $\text{Na}_2\text{HPO}_4$  solution was added into cosolution; (d) AS was originally in the random coil conformation; (e) Calcium ions were bound to the anionic side-chains of AS; (f) The nucleation of HAp was initiated after addition of  $\text{Na}_2\text{HPO}_4$  solution.

first extracted aqueous AS from *A. pernyi* cocoon (Figure 1A). The amino acid analysis (Table S1) indicated that AS contains the acidic amino acid such as Glu and Asp, which are considered as the sites for triggering HAp nucleation on silk fibroin and BS.<sup>20–23</sup> Thus we anticipated that AS could control the nucleation of HAp in the presence of  $\text{Ca}^{2+}$  and  $\text{PO}_4^{3-}$ . As described in Figure 1B, the anionic side-chains of AS first bind  $\text{Ca}^{2+}$  through electrostatic attraction, which further attracts  $\text{PO}_4^{3-}$  to initiate the nucleation of HAp and in turn promotes the assembly of AS and HAp into clusters (Figure 1C). It was found that HAp could promote the osteogenic differentiation of BMSCs,<sup>8,9</sup> so we hypothesized that mineralized AS would improve cell viability and osteogenic differentiation due to the presence of bone minerals in the resultant materials. To test this hypothesis, we studied the effect of mineralization of AS on the cell viability and on the osteogenic differentiation of the human bone marrow derived mesenchymal stem cells (BMSCs; Figure 1D).

## 2. MATERIALS AND METHODS

**2.1. Materials.** *A. pernyi* silkworm cocoons were purchased from Shandong Academy of Sericulture, China.  $\text{CaCl}_2$ ,  $\text{Na}_2\text{HPO}_4$ ,  $\text{NaHCO}_3$ , and other reagents of analytical grade were purchased from Sinopharm Chemical Reagents Co. Ltd., China. Deionized water was used throughout the experiment. Fetal bovine serum (FBS) and 0.25% trypsin were purchased from Invitrogen. Dulbecco's modified Eagle's medium (DMEM) and 1% penicillin-streptomycin were purchased from Gibco.

**2.2. Preparation of AS Solution.** The aqueous AS solution was prepared from *A. pernyi* silkworm cocoons according to the reported procedure.<sup>24</sup> *A. pernyi* cocoons were cut into small pieces and heated in deionized water at 120 °C for 30 min in an autoclave as described in Figure 1A. After that, the solution was centrifuged at 6000 rpm for 10 min. The aqueous AS solution was obtained by collecting the supernatant. The final concentration of AS solution was calculated by weighing the remaining solid after drying. The concentrations of aqueous AS solutions were varied from 0.5 to 8 mg/mL for the following experiments.

**2.3. Biominerilization of AS Solution.** Nucleation of HAp mediated by AS solution was performed by a wet precipitation method described in the previous paper.<sup>17</sup> In order to investigate the effect of AS concentration and mineralization time on the nucleation of HAp, the concentrations of AS were controlled to be 0.5, 2, and 8 mg/mL, and the mineralization time was set at 2, 6, 12, and 24 h, respectively. To investigate the role of AS concentration in HAp nucleation,  $\text{CaCl}_2$  was first added into 100 mL of AS solution with various concentrations of 0.5, 2, and 8 mg/mL, respectively, and mixed completely. The concentration of  $\text{CaCl}_2$  was controlled at 20 mM. Subsequently, 100 mL of 12 mM  $\text{Na}_2\text{HPO}_4$  was added into above cosolution at a rate of 5 mL/min controlled by a constant flow pump. This aqueous solution system was stirred to allow the HAp nucleation on AS. The mineralization time was controlled at 24 h. The pH value of this aqueous solution system was adjusted to a constant value of 9.5 by adding 0.1 M NaOH solution. After the mineralization was finished, the aqueous solution system was centrifuged at 6000 rpm for 10 min. The mineralized AS was collected by gathering the precipitation followed by washing it with deionized water three times. In addition, to find out whether mineralization of AS is dependent on time, the same procedure was performed on AS with concentration of 2 mg/mL by controlling the mineralization time at 2, 6, 12, and 24 h, respectively. The resultant mineralized AS (MAS) was named as MAS<sub>2</sub>, MAS<sub>6</sub>, MAS<sub>12</sub>, and MAS<sub>24</sub>, respectively.

### 2.4. Characterization of HAp Nucleation Mediated by AS.

TEM was used to observe the nucleation of HAp under different concentrations of AS and mineralization times. The aqueous solution system was sonicated for 10 min and 10  $\mu\text{L}$  of this solution was dropped onto the copper grids. After dried in air, the sample was washed by deionized water twice to remove any soluble salts. Transmission electron microscopy (TEM) and high-resolution transmission electron microscopy (HR-TEM) were carried out on JEOL JEM-1200EX and FEI Tecnai G2F30, respectively. In order to only observe the morphology of HAp in the mineralized composites, the composites were not stained before TEM imaging. X-ray diffraction (XRD) and Fourier transform infrared (FT-IR) spectroscopic measurements were performed to confirm the formation of HAp. For XRD, X-ray diffraction patterns of AS and mineralized AS were measured by X' Pert PRO diffractometer. The powder samples were scanned in the range of 10° to 60°. FT-IR spectra were recorded using a Fourier transform infrared spectrometer (FTIR-8400S, Shimadzu, Japan). A total of 2 mg AS or mineralized AS were mixed with 200 mg KBr and then pressed into discs, respectively. The measurements were performed with the wavenumber ranging from 400 to 4000  $\text{cm}^{-1}$ .

**2.5. Assembly Structure of Mineralized AS.** The assembly structure of mineralized AS was observed with atomic force microscopy (AFM, MultiMode, VEECO, U.S.A.) in tapping mode. For AFM, the concentration of aqueous solution system was diluted to be  $1 \times 10^{-2}$  mg/mL by deionized water. Four  $\mu\text{L}$  of this diluted

**Table 1.** Primer Sequences Used for Quantitative Reverse Transcription-Polymerase Chain Reaction Gene Expression Analysis

genes	5'-3'	primers	product size (bp)
Smad8	forward	CACGGCTTGAAAGTCGTGTAT	198
	reverse	TGAAGAAATGGGGTTATGTGGA	
Runx2	forward	GTGATAAATTCAAGAAGGGAGG	118
	reverse	CTTTTGCTAATGCTTCGTGT	
osteocalcin	forward	AGGGCAGCGAGGTAGTGAAGA	181
	reverse	TAGACCGGGCCGTAGAACG	
integrin a2	forward	CCGACAGGGTTATCATAGGCA	224
	reverse	CATTCAACCACACCAGCGAGC	
PPAR $\gamma$	forward	TTCTCCTATTGACCCAGAAAGC	307
	reverse	CTCCACTTGGATTGCACCTTGG	

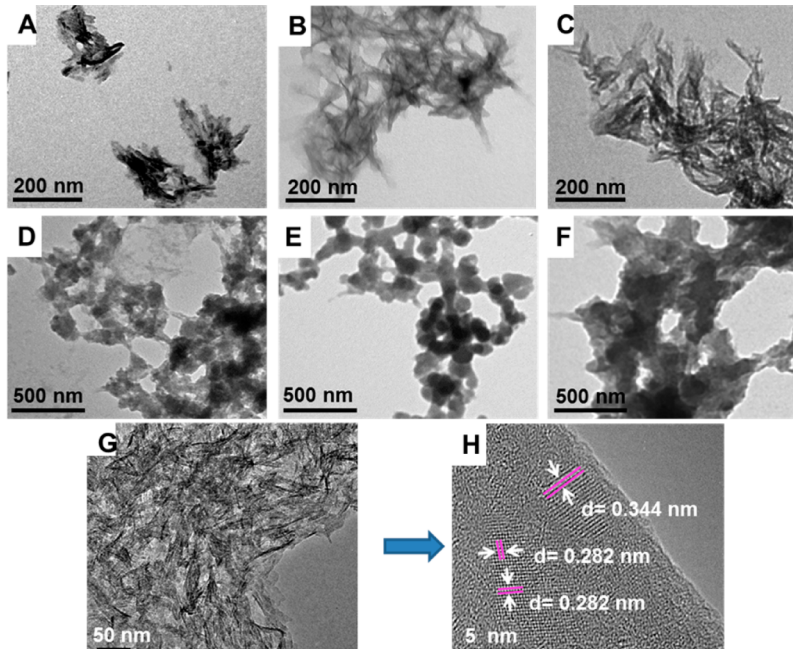


**Figure 2.** TEM images showing the nucleation of HApS mediated by AS with different concentrations and mineralization times. (A–C) The mineralization time was 24 h, but the concentration of AS was set at (A) 0.5, (B) 2, and (C) 8 mg/mL; (D–F) The concentration of AS was fixed at 2 mg/mL, but the mineralization time was chosen at (D) 2, (E) 6, and (F) 12 h; (G) HRTEM image showing the nanoneedles of HApS mediated by AS with the concentration of 2 mg/mL after mineralization for 24 h; and (H) is a high magnification image of (G). White arrows show the lattice spacings of 0.344 and 0.282 nm, which are corresponding to the  $d$ -spacings of (002) and (211) lattice planes, respectively.

solution was deposited on freshly cleaved mica and air-dried, followed by washing with 20  $\mu$ L deionized water. The images were taken and processed by software (NanoScope Image). In addition, the secondary structure of AS before and after mineralization was observed by circular dichroism (CD) with the concentration of 0.1 mg/mL at room temperature. The CD measurement was performed between 190 and 250 nm with a MOS-450 spectrometer (Biologic, France) using a quartz cell with a path length of 1 mm. The reported CD pattern represents an average of three consecutive scans measured at the rate of 0.5 nm/s.

**2.6. Cell Viability Assay on AS and Mineralized AS.** We used human BMSCs as testing cells. Human BMSCs were isolated as described in our previous work.<sup>25,24</sup> Cells at the fourth to sixth passage were used for experiment. BMSCs were cultured in DMEM with 10% FBS and 1% penicillin-streptomycin. Medium was changed every 3 days. MAS<sub>24</sub> was used as MAS for cell viability test. The empty well and BS were used as control, respectively. The BS, AS, and MAS solutions (100  $\mu$ L) were added to 96-well microplates, respectively, and then desiccated under vacuum for 24 h. This process allowed the BS, AS, and MAS to form a film on the well of microplates. Each well was sterilized by 75% (V/V) ethanol, and washed with physiological saline three times. BMSCs ( $10^4$  cells/cm<sup>2</sup>) were seeded on the BS, AS,

and MAS films, respectively, and cultured in DMEM supplemented with 10% fetal bovine serum in a 5% CO<sub>2</sub> incubator at 37 °C.

After 1, 3, and 7 days culture, cell morphology observation was performed by fixing specimens in 4% formalin solution for 15 min and 1% Triton X-100 in PBS for 10 min. The cytoskeletons were visualized by actin (F-actin was detected using TRITC-conjugated Phalloidin; Millipore), and cell nuclei were visualized by DAPI (Beyotime Institute of Biotechnology, China). The cells were viewed under confocal microscope system (Olympus FV1000, Japan). In addition, the cell viability on AS and mineralized AS was determined by using Cell Counting Kit-8 (CCK-8, Dojindo). After culture of 1, 3, and 7 days, the cells were incubated in 10% CCK-8 solution in a 5% CO<sub>2</sub> incubator at 37 °C for 2 h. The intense orange-colored formazan derivative formed by cell metabolism is soluble in the culture medium. The absorbance of the culture medium was detected at 450 nm using a microplate reader (Bio-Rad 680, U.S.A.). Cell number was correlated to optical density (OD).

**2.7. Osteogenic Differentiation of BMSCs on AS and Mineralized AS.** Human BMSCs culture was described above. Cells at the fourth to sixth passage were used for experiment. BS was used as a control. Films were cast from aqueous solutions of AS, MAS, and BS. BMSCs ( $10^4$  cells/cm<sup>2</sup>) were seeded onto the films and cultured in osteogenic induction medium. After 2 weeks, the levels of mRNA for

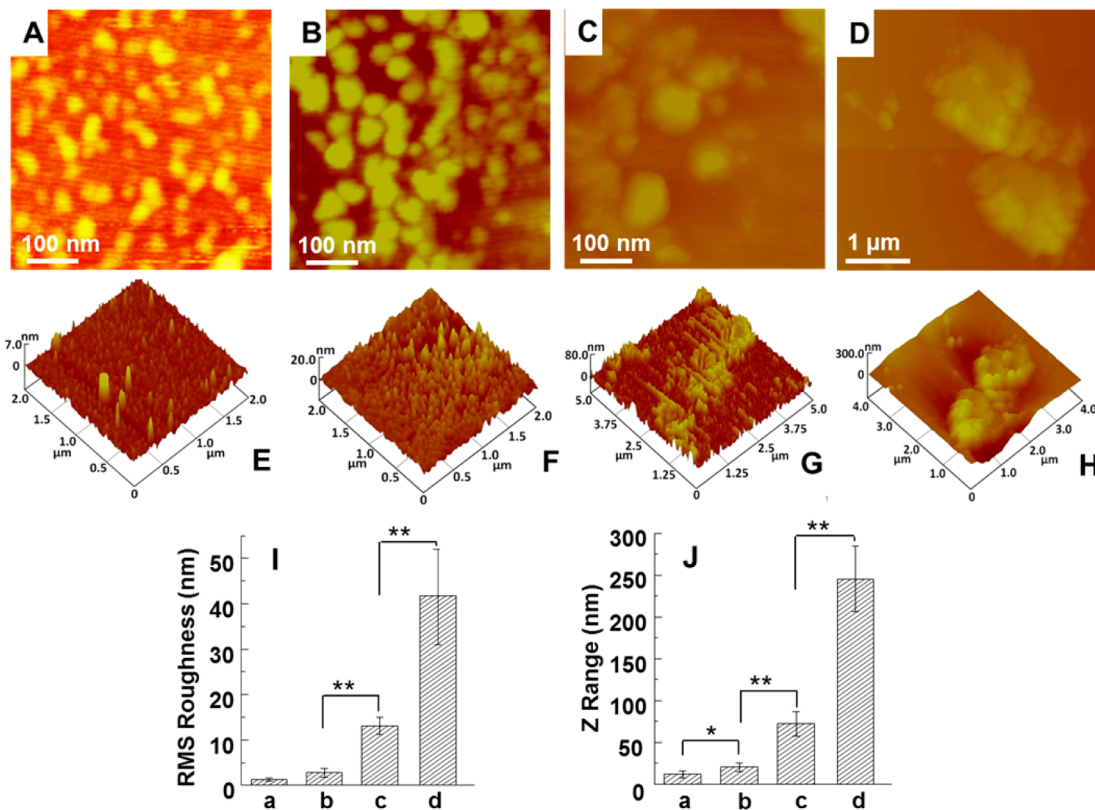


**Figure 3.** Topographies of AFM images and corresponding section analysis of AS and mineralized AS (MAS): (A) AS, (B) MAS<sub>2</sub>, (C) MAS<sub>6</sub>, (D) MAS<sub>24</sub>; (E–H) three-dimensional images corresponding to (A–D), respectively; (I, J) histograms of RMS roughness and z range; (a–d) in I and J are the samples corresponding to (A–D), respectively. MAS<sub>2</sub>, MAS<sub>6</sub>, and MAS<sub>24</sub> represent AS after mineralized for 2, 6, and 24 h, respectively.

osteogenic specific genes (Smad 8, Runx2, and OCN), integrin (integrin  $\alpha 2$ ), and adipose marker (PPAR $\gamma$ ) of BMSCs cultured on the AS, MAS, and BS films in the osteogenic medium were assessed using real-time PCR. Total cellular RNA was extracted by lysis in trizol (Invitrogen). PCR was performed using Brilliant SYBR Green QPCR Master Mix (TakaRa) with a Light Cycler apparatus (ABI 7900HT). The PCR cycling consisted of 40 cycles of amplification of the template DNA with primer annealing at 60 °C. The relative level of expression of each target gene was then calculated using the  $2^{-\Delta\Delta Ct}$  method.<sup>26</sup> The amplification efficiencies of primer pairs were validated to enable quantitative comparison of gene expression. All primers (Invitrogen) were designed using primer 5.0 software and are listed in Table 1. Each real-time PCR was performed on four different experimental samples and representative results are shown as target gene expression normalized to reference gene GAPDH.<sup>27</sup>

Alkaline phosphatase (ALP) and alizarin red staining were also performed to investigate BMSCs differentiation. BMSCs ( $10^4/\text{cm}^2$ ) were seeded onto the AS and MAS film and cultured in osteogenic induction medium. After 2 weeks, ALP activity was assayed using a BCIP/NBT alkaline phosphatase color development kit (Beyotime Institute of Biotechnology). The ALP staining was observed under an optical microscope (Olympus IX71, Japan). Calcium deposits were detected by staining with 2% alizarin red S (pH 4.2; Sigma). To quantify the stained nodules, the stain was solubilized with 0.5 mL 5% sodium dodecyl sulfate (SDS) in 0.5N HCl for 30 min at room temperature. Solubilized stain was transferred to wells of a 96-well plate, and absorbance was measured at 405 nm.<sup>28</sup> The final absorbance was obtained by subtracting the absorbance of corresponding wells containing the same scaffolds but without cells seeded in order to remove the contribution from the minerals in the mineralized scaffolds.

**2.8. Statistical Analysis.** Data were presented as mean values  $\pm$  standard deviation (SD),  $n = 4$ . Statistical differences among the samples were determined by two tailed, unpaired student  $t$  test.

Differences between groups were considered statistically significant at  $p < 0.05$  and highly significant at  $p \leq 0.01$ .

### 3. RESULTS AND DISCUSSION

**3.1. Nucleation of HApS Mediated by AS.** The nucleation of HApS on *B. mori* fibroin and sericin is triggered by anionic side-chains that bind Ca<sup>2+</sup>.<sup>9,17,29</sup> This implies that the amount of acidic amino acid of AS can affect the nucleation HApS. Therefore, we expected that the concentration of AS can impact the nucleation of HApS because the amount of acidic amino acids is dependent on the concentration. We used three different AS concentrations (0.5, 2, and 8 mg/mL) to investigate the effect of AS concentration on the nucleation of HApS. The TEM images show that AS concentration can mediate the morphology of HApS (Figure 2A–C). HApS were grown into nanoneedle-like morphology when the AS concentration was 0.5 mg/mL (Figure 2A). When the AS concentration was increased to 2 mg/mL, the length of the nanoneedles was increased (Figure 2B). Aggregation of HApS were clearly observed at the AS concentration of 8 mg/mL (Figure 2C). This result confirmed that concentration indeed plays an important role in the nucleation of HApS, implying that a higher concentration of AS was in favor of nanoneedle-like crystal formation.

The effect of mineralization time on the nucleation of HApS was described in Figure 2D–F. On MAS<sub>2</sub>, a clump of starfish-like crystals was randomly scattered, indicating that AS provided nucleation sites for crystal growth (Figure 2D). On MAS<sub>6</sub>, spherical crystals were formed and aggregated (Figure 2E). When the mineralization time was increased to 12 h (MAS<sub>12</sub>), spindly crystals were heavily aggregated (Figure 2F).

HRTEM image of  $\text{MAS}_{24}$  (Figure 2G) indicated that nanoneedle crystals were grown after mineralization for 24 h (Figure 2G). The size of nanoneedle crystals was approximately 20 to 40 nm in length and 3 to 5 nm in width. The lattice spacing of 0.344 and 0.282 nm in Figure 2H proved the nucleation of HAp as they are corresponding to the *d*-spacing of (002) and (211) lattice planes of HAp, respectively.<sup>30,31</sup> These results proved that the nucleation of HAp mediated by AS is a gradual process, which is in agreement with our proposed mechanism on HAp nucleation as described in Figure 1B.

In addition, the nucleation of HAp was verified by XRD and FT-IR measurements. The sharp peaks at  $25.9^\circ$  and  $32.1^\circ$  assigned to the planes (002) and (211) of HAp were observed in Figure S1. The intensity of these two peaks was increased with increase in the mineralization time, indicating the mineralization time can affect the growth of HAp. The peaks of 561, 602, and  $1030\text{ cm}^{-1}$  at FT-IR spectra (Figure S2) proved the nucleation of HAp. The peaks of 561 and  $602\text{ cm}^{-1}$  are corresponding to the O-P-O stretching vibration while the peak at  $1030\text{ cm}^{-1}$  can be assigned to the P-O stretching vibration of HAp.<sup>6</sup> XRD and FT-IR results further confirm the formation of HAP observed by TEM. In addition, the peak for the amide II in the FT-IR spectra is shifted from  $1540$  to  $1525\text{ cm}^{-1}$ , indicating that AS are assembled into  $\beta$ -sheet with the nucleation of HAp.

**3.2. Assembly Structure of Mineralized AS.** We hypothesized that the  $\text{Ca}^{2+}$  chelated AS would attract  $\text{PO}_4^{3-}$  to initiate the nucleation of HAp and simultaneously to drive  $\beta$ -sheet assembly of AS due to hydrogen bond interaction. TEM observation shows that HAp are nucleated and their morphologies are changed from spindly to nanoneedle-like (Figure 2). AFM was also used to observe the assembly structure of AS during HAp growth. Figure 3A–D are the topographies of AS,  $\text{MAS}_2$ ,  $\text{MAS}_6$ , and  $\text{MAS}_{24}$ , respectively. Figure 3E–H are the 3D AFM images corresponding to Figure 3A–D, respectively. The results of statistical analysis of RMS roughness and Z range of AS,  $\text{MAS}_2$ ,  $\text{MAS}_6$ , and  $\text{MAS}_{24}$  are indicated in Figure 3I and J, respectively.

Prior to mineralization, AS appeared to be individual globules (Figure 3A), similar to the morphology of BS.<sup>32</sup> AS was homogeneously distributed on the surface of mica substrate due to the Brownian motion (Figure 3E).<sup>33</sup> Its RMS roughness was  $1.5 \pm 0.3\text{ nm}$  (Figure 3I-a), and the z range was  $11.5 \pm 3.2\text{ nm}$  (Figure 3J-a), suggesting that AS formed a flat surface. After mineralization of 2 h, the individual globules were enlarged and the height was increased (Figure 3B,F). The cluster patterns tended to be aggregated in the case of  $\text{MAS}_6$ . With the mineralization time increased to 24 h, larger aggregation was formed with a diameter of  $2\text{ }\mu\text{m}$ . Correspondingly, the RMS roughness was significantly increased to  $41.7 \pm 11.2\text{ nm}$  (Figure 3I), and the z range to  $245.2 \pm 35.2\text{ nm}$ , respectively (Figure 3J). AFM images clearly demonstrate that AS and HAp are assembled into globules, verifying the self-assembly of AS during mineralization as anticipated in Figure 1B,C.

CD spectra proved the  $\beta$ -sheet assembly of AS through mineralization (Figure 4). AS adopts a random coil conformation according to a maximum degree of negative ellipticity at about 198 nm (Figure 4A). After mineralization, the appearance of the maximum degrees of positive ellipticity at 190 nm and the negative ellipticity at 216 nm (Figure 4B) proved the  $\beta$ -sheet structure of AS, indicating that AS can

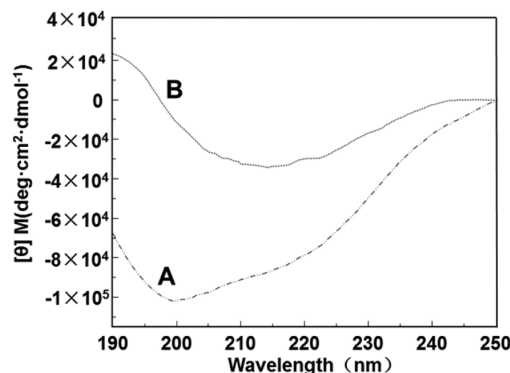


**Figure 4.** CD spectra of AS and mineralized AS: (A) aqueous AS solution and (B) AS solution after mineralization for 24 h. CD spectra show that the structure of AS is transited from random coil to  $\beta$ -sheet after mineralization.

trigger the nucleation of HAp whereas the presence of  $\text{Ca}^{2+}$  and  $\text{PO}_4^{3-}$  can induce  $\beta$ -sheet assembly of AS.

**3.3. Cell Viability of Mineralized AS.** To determine the effect of the scaffolds on supporting cell growth, we seeded BMSCs on BS, AS and MAS, and then examined the morphology by immunofluorescence for 1 (Figure 5A), 3 (Figure S3), and 7 days (Figure 5B), and measured cell proliferation ability by CCK-8 assay (Figure 5C). The confocal micrographs indicated that BMSCs were of more spindle shape on BS and AS (Figure 5a,d,j,m), while most of BMSCs exhibited a more stellate-patterned phenotype on MAS (Figure 5g,p). It means cells spread widely on the MAS with distinct spread actin filaments compared to those on the AS and BS. This result illustrated that MAS could support cell adhesion and spreading. After 7 days culturing, there were plenty of BMSCs on AS and MAS, whereas fewer cells were observed on the BS (Figure 5B). Cell proliferation analysis by CCK-8 further confirmed that the proliferation rate on AS and MAS is higher than that on BS, and MAS shows higher proliferation rate than AS. Therefore, the CCK-8 assay results indicated that MAS promoted proliferation of BMSCs during the early period of cell culture, proving that mineralization of AS improves the cell viability of AS. It suggests that MAS can be used as a biocompatible biomaterial to support cell growth.

**3.4. Osteogenic Differentiation of BMSCs on Mineralized AS.** To examine the effect of MAS, AS, and BS on osteogenic differentiation of BMSCs, we examined gene expression profile of BMSCs in the osteogenic induction culture (Figure 6). The transcript levels of osteogenic marker genes including Smad8, OCN, and Runx2 were investigated. Expression of Smad8, OCN, and Runx2 was higher on MAS than that on AS and BS, suggesting MAS promoted the osteogenic differentiation of BMSCs. In addition, the expression of integrin, the major adhesion receptor that mediates cell adhesion and attachment,<sup>34</sup> was compared among different substrates, according to its subunits, Integrin  $\alpha 2$  (Itga2). The expression of Itga2 was remarkably up-regulated in BMSCs culture on MAS. Conversely, peroxisome proliferator-activated receptor  $\gamma$  (PPAR $\gamma$ ), the adipose marker, was down-regulated when BMSCs were grown on MAS compared to that on AS and BS, indicating that BMSCs differentiation into adipogenic lineage was suppressed on MAS.

ALP staining and alizarin red staining further confirmed the real-time PCR results. Higher levels of ALP activities were also observed on MAS than on AS and BS from ALP staining

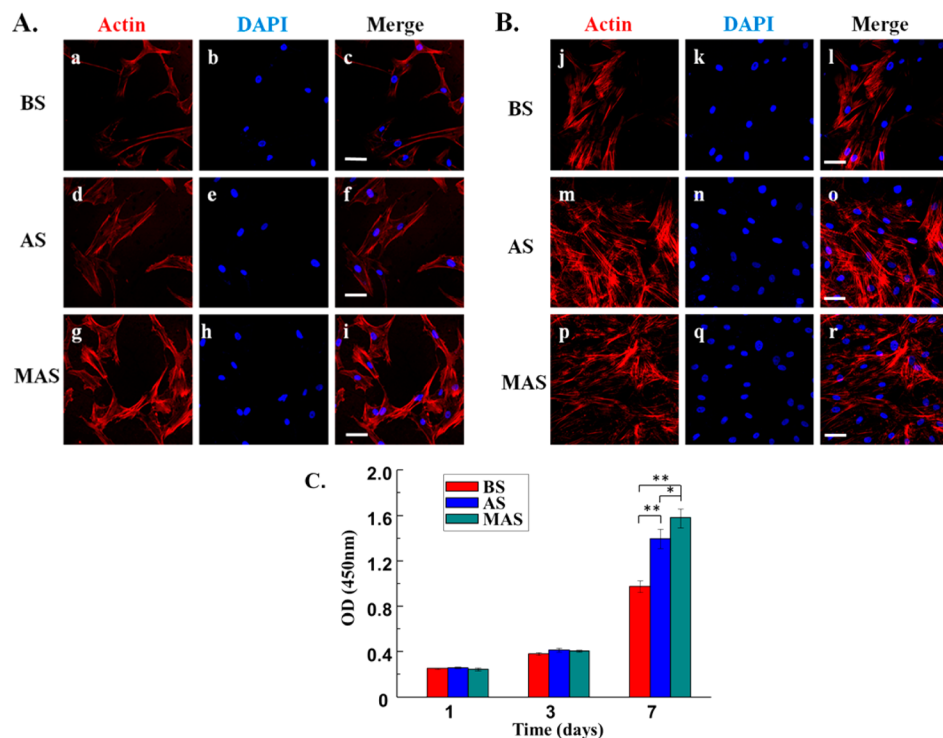


**Figure 5.** Morphology and proliferation of human BMSCs on scaffolds. (A, B) Morphology of human BMSCs on BS, AS, and MAS after cultured for 1 day and 7 days; Cell skeleton staining with Actin (red); (a, d, g, j, m, p) Nuclear staining with DAPI (blue); (b, e, h, k, n, q) Merged images (c, f, i, l, o, r). The BMSCs were adherent and proliferated strongly on MAS and AS. (C) BMSCs proliferation on plate, BS, AS, and MAS. Scale bars, 50  $\mu$ m; \* $P < 0.05$ , \*\* $P < 0.01$ . Blank means empty well without coating. BS, AS, and MAS denote well coated with *B. mori* sericin, *A. pernyi* sericin, and mineralized *A. pernyi* sericin, respectively.

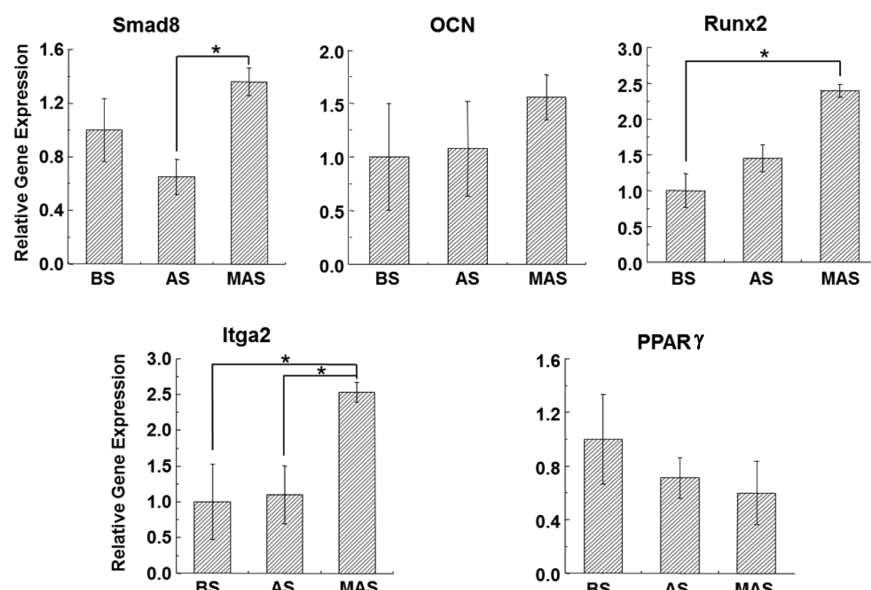


**Figure 6.** Levels of mRNA for osteogenic specific genes (Smad8, OCN, and Runx2), integrin (Itga2), and adipose marker PPAR $\gamma$  of h-BMSCs cultured on BS, AS, and MAS in osteogenic medium for 2 weeks. The mRNA levels were quantified using real-time RT-PCR and are normalized to that of the reference gene GAPDH and compared to that of BS groups. \* $P < 0.05$ , data are presented as mean  $\pm$  SD,  $n = 4$ . BS, AS and MAS mean *B. mori* sericin, *A. pernyi* sericin, and mineralized *A. pernyi* sericin, respectively.

images after 2 weeks of induction (Figure 7A). Quantitative analysis from alizarin red S staining shows the significant difference between MAS and AS ( $P < 0.01$ ) as well as BS ( $P < 0.01$ ; Figure 7B). Taken together, these data confirmed that MAS promoted the differentiation of BMSCs into osteoblasts in comparison to AS and BS.

The fate of BMSCs could be directed by the compositions and structures of the substrates.<sup>35,36</sup> In particular, the effect of HAs on osteogenic differentiation of BMSCs has been reported.<sup>37–39</sup> It was found that HAs promoted osteogenic differentiation through early upregulation of osteopontin (OPN) and later upregulation of osteocalcin (OCN) and

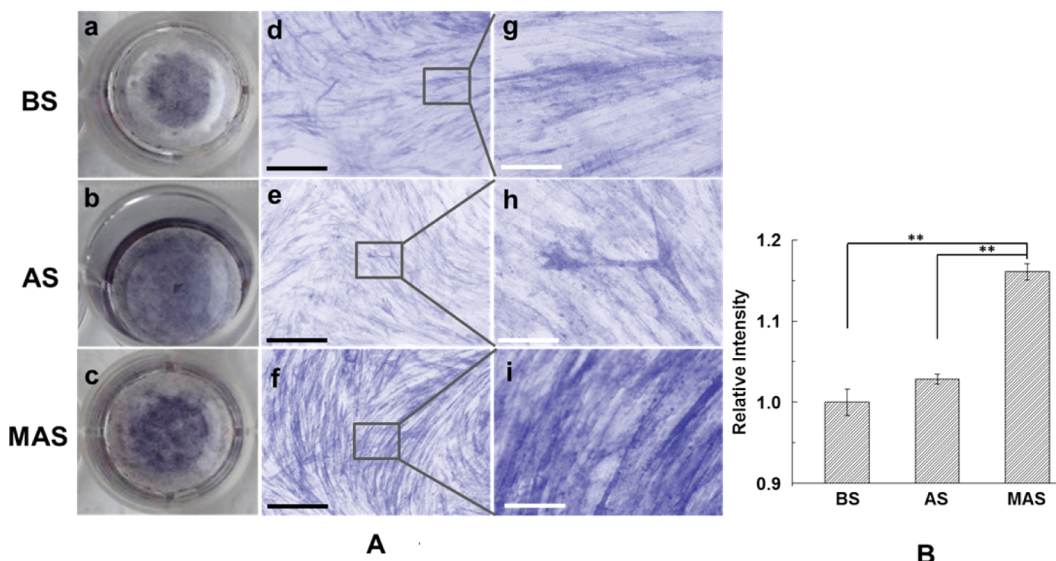


**Figure 7.** ALP staining and alizarin red staining of BMSCs cultured on BS, AS and MAS in osteogenic medium for 2 weeks: (A) ALP staining of BMSCs cultured on MAS; (B) The quantification result of alizarin red staining determined by absorbance at 405 nm; (a–c) are macroscopic view of ALP staining of BMSCs on BS, AS, and MAS, whereas (d–i) are microscopic view of ALP staining of BMSCs on (d, g) BS, (e, h) AS, and (f, i) MAS. Black scale bars = 500  $\mu$ m, white scale bars = 200  $\mu$ m. \*\* $P$  < 0.01, data are presented as mean  $\pm$  SD,  $n$  = 4. BS, AS, and MAS were *B. mori* sericin, *A. pernyi* sericin, and mineralized *A. pernyi* sericin.

bone sialoprotein (BSP) in a 3D model system, relative to noncoated controls.<sup>37</sup> Scaffolds impregnated with HApS increased in vitro bone nodule formation, as well as in vivo bone formation,<sup>38</sup> providing an appropriate osteogenic environment for tissue engineering.<sup>39</sup> The mineralization of silk fibroin scaffolds provides increased osteoconductive environment for BMSCs to construct tissue engineered bone to repair mandible defects in large animal.<sup>8–10</sup> In this work, we confirmed that AS can mediate the nucleation of HApS according to Figures 2–4. The proliferation rate on AS is higher than that on BS, and MAS shows higher proliferation rate than AS (Figure 5). This might be due to their different composition. The results from Figures 6 and 7 also suggested that compared to AS and BS, MAS significantly enhanced osteogenic differentiation of BMSCs by activating integrin signaling pathway, but inhibited the adipogenic differentiation of BMSCs by repressing adipose marker gene. Therefore, we concluded that AS with incorporation of HApS promotes osteogenic differentiation of BMSCs, which provides an appropriate osteoconductive environment for BMSCs. Mineralization of AS is a useful biomimetic route to enhance the osteoconductivity conditions of AS for BMSCs. The mineralized AS would have potential application in the bone tissue engineering.

#### 4. CONCLUSIONS

To explore the biomaterials based on silk sericin extracted from wild silkworm, *A. pernyi* silkworm, this study investigated the mineralization of AS and its use in promoting osteogenic differentiation of BMSCs. It was found that AS mediated the mineralization in a wet precipitation method. The nucleation of HApS was controlled by AS concentration and mineralization time as evidenced by TEM, XRD, and FTIR results. HApS were nucleated into nanoneedles according to HRTEM images. AFM and CD observation proved that AS mediated HApS nucleation while self-assembling into  $\beta$ -sheets, and finally mineralized AS was assembled into globule aggregation. The mineralized AS could be cast into films to support cell growth

and improve the cell attachment and proliferation due to incorporation of HApS. Most importantly, we found that mineralization of AS promoted osteogenic differentiation of BMSCs, representing the first report on the osteogenic differentiation of BMSCs on silk sericin. The mineralization of *A. pernyi* silk sericin coupled with its biocompatibility and capability in promoting osteogenic differentiation of BMSCs proved that *A. pernyi* silk sericin would have potential applications in the field of bone tissue engineering. Our work will lay foundation for the use of *A. pernyi* silk sericin as a potential scaffold material in tissue engineering.

#### ■ ASSOCIATED CONTENT

##### S Supporting Information

Figure S1, XRD patterns of samples; Figure S2, FTIR spectra of samples; Figure S3, EDX spectra of samples; Table S1: The amino acid composition analysis of AS. This material is available free of charge via the Internet at <http://pubs.acs.org>.

#### ■ AUTHOR INFORMATION

##### Corresponding Authors

\*E-mail: cbmao@ou.edu.

\*E-mail: yangm@zju.edu.cn.

##### Author Contributions

<sup>†</sup>These authors contributed equally to this work (M.Y., Y.S., and C.Z.).

##### Notes

The authors declare no competing financial interest.

#### ■ ACKNOWLEDGMENTS

M.Y. acknowledges the support of National High Technology Research and Development Program 863 (2013AA102507), Zhejiang Provincial Natural Science Foundation of China (LZ12C17001), National Natural Science Foundation of China (20804037 and 21172194), and Silkworm Industry Science and Technology Innovation Team (2011R50028). Y.Y. would like to thank the financial support from Projects of Zhejiang

Provincial Science and Technology Plans (2012C12910). C.B.M. would like to thank the financial support from National Institutes of Health (EB015190 and HL092526), National Science Foundation (CBET-0854465, CMMI-1234957, CBET-0854414, and DMR-0847758), Department of Defense Peer Reviewed Medical Research Program (W81XWH-12-1-0384), Oklahoma Center for Adult Stem Cell Research (434003), and Oklahoma Center for the Advancement of Science and Technology (HR11-006).

## ■ REFERENCES

- (1) Denissen, H.; De Groot, K.; Makkes, P. C.; Van den Hooff, A.; Klopper, P. Tissue response to dense apatite implants in rats. *J. Biomed. Mater. Res.* **1980**, *14* (6), 713–721.
- (2) Rai, R. K.; Sinha, N. Dehydration-induced structural changes in the collagen–hydroxyapatite interface in bone by high-resolution solid-state NMR spectroscopy. *J. Phys. Chem. C* **2011**, *115* (29), 14219–14227.
- (3) Shchukin, D. G.; Sukhorukov, G. B.; Möhwald, H. Biomimetic fabrication of nanoengineered hydroxyapatite/polyelectrolyte composite shell. *Chem. Mater.* **2003**, *15* (20), 3947–3950.
- (4) Rodrigues, C.; Serricella, P.; Linhares, A.; Guerdes, R.; Borojevic, R.; Rossi, M.; Duarte, M.; Farina, M. Characterization of a bovine collagen–hydroxyapatite composite scaffold for bone tissue engineering. *Biomaterials* **2003**, *24* (27), 4987–4997.
- (5) Biswas, A.; Bayer, I. S.; Zhao, H.; Wang, T.; Watanabe, F.; Biris, A. S. Design and synthesis of biomimetic multicomponent all-bone-minerals bionanocomposites. *Biomacromolecules* **2010**, *11* (10), 2545–2549.
- (6) Liu, L.; Liu, J.; Wang, M.; Min, S.; Cai, Y.; Zhu, L.; Yao, J. Preparation and characterization of nano-hydroxyapatite/silk fibroin porous scaffolds. *J. Biomater. Sci.* **2008**, *19* (3), 325–338.
- (7) Lin, F.; Li, Y.; Jin, J.; Cai, Y.; Wei, K.; Yao, J. Deposition behavior and properties of silk fibroin scaffolds soaked in simulated body fluid. *Mater. Chem. Phys.* **2008**, *111* (1), 92–97.
- (8) He, T.; Abbineni, G.; Cao, B.; Mao, C. B. Nanofibrous bio-inorganic hybrid structures formed through self-assembly and oriented mineralization of genetically engineered phage nanofibers. *Small* **2010**, *6*, 2230–2235.
- (9) Wang, F.; Cao, B.; Mao, C. B. Bacteriophage bundles with pre-aligned  $\text{Ca}^{2+}$  initiate the oriented nucleation and growth of hydroxyapatite. *Chem. Mater.* **2010**, *22*, 3630–3636.
- (10) Xu, H.; Cao, B.; George, A.; Mao, C. B. Controlled self-assembly and mineralization of genetically modifiable nanofibers driven by beta-structure formation. *Biomacromolecules* **2011**, *12*, 2193–2199.
- (11) He, P.; Sahoo, S.; Ng, K. S.; Chen, K.; Toh, S. L.; Goh, J. C. H. Enhanced osteoinductivity and osteoconductivity through hydroxyapatite coating of silk-based tissue-engineered ligament scaffold. *J. Biomed. Mater. Res.* **2013**, *A101* (2), 555–566.
- (12) He, P.; Ng, K. S.; Toh, S. L.; Goh, J. C. H. In vitro ligament–bone interface regeneration using a trilineage coculture system on a hybrid silk scaffold. *Biomacromolecules* **2012**, *13* (9), 2692–2703.
- (13) Wang, G.; Yang, H.; Li, M.; Lu, S.; Chen, X.; Cai, X. The use of silk fibroin/hydroxyapatite composite co-cultured with rabbit bone-marrow stromal cells in the healing of a segmental bone defect. *J. Bone Joint Surg.* **2010**, *92* (2), 320–325.
- (14) Zhang, Y.-Q. Applications of natural silk protein sericin in biomaterials. *Biotechnol. Adv.* **2002**, *20* (2), 91–100.
- (15) Zhaorigetu, S.; Sasaki, M.; Kato, N. Consumption of sericin suppresses colon oxidative stress and aberrant crypt foci in 1,2-dimethylhydrazine-treated rats by colon undigested sericin. *J. Nutr. Sci. Vitaminol.* **2007**, *53* (3), 297–300.
- (16) Kundu, S. C.; Dash, B. C.; Dash, R.; Kaplan, D. L. Natural protective glue protein, sericin bioengineered by silkworms: potential for biomedical and biotechnological applications. *Prog. Polym. Sci.* **2008**, *33* (10), 998–1012.
- (17) Kaur, J.; Rajkhowa, R.; Tsuzuki, T.; Millington, K.; Zhang, J.; Wang, X.-G. Photo-protection by silk cocoons. *Biomacromolecules* **2013**, *14* (10), 3660–3667.
- (18) Nishida, A.; Yamada, M.; Kanazawa, T.; Takashima, Y.; Ouchi, K.; Okada, H. Sustained-release of protein from biodegradable sericin film, gel and sponge. *Int. J. Pharm.* **2011**, *407* (1), 44–52.
- (19) Cai, Y.; Jin, J.; Mei, D.; Xia, N.; Yao, J. Effect of silk sericin on assembly of hydroxyapatite nanocrystals into enamel prism-like structure. *J. Mater. Chem.* **2009**, *19* (32), 5751–5758.
- (20) Takeuchi, A.; Ohtsuki, C.; Miyazaki, T.; Kamitakahara, M.; Ogata, S.-i.; Yamazaki, M.; Furutani, Y.; Kinoshita, H.; Tanihara, M. Heterogeneous nucleation of hydroxyapatite on protein: structural effect of silk sericin. *J. R. Soc., Interface* **2005**, *2* (4), 373–378.
- (21) Kong, X.; Cui, F.; Wang, X.; Zhang, M.; Zhang, W. Silk fibroin regulated mineralization of hydroxyapatite nanocrystals. *J. Cryst. Growth* **2004**, *270* (1), 197–202.
- (22) Cheng, C.; Shao, Z.; Vollrath, F. Silk fibroin regulated crystallization of calcium carbonate. *Adv. Funct. Mater.* **2008**, *18* (15), 2172–2179.
- (23) Takeuchi, A.; Ohtsuki, C.; Miyazaki, T.; Tanaka, H.; Yamazaki, M.; Tanihara, M. Deposition of bone-like apatite on silk fiber in a solution that mimics extracellular fluid. *J. Biomed. Mater. Res.* **2003**, *A65* (2), 283–289.
- (24) Padamwar, M. N.; Pawar, A. P.; Daithankar, A. V.; Mahadik, K. Silk sericin as a moisturizer: an in vivo study. *J. Cosm. Derm.* **2005**, *4* (4), 250–257.
- (25) Zou, X. H.; Cai, H. X.; Yin, Z.; Chen, X.; Jiang, Y. Z.; Hu, H.; Ouyang, H. W. A novel strategy incorporated the power of mesenchymal stem cells to allografts for segmental bone tissue engineering. *Cell Transplant.* **2009**, *18* (4), 433–441.
- (26) Livak, K. J.; Schmittgen, T. D. Analysis of relative gene expression data using real-time quantitative PCR and the  $2(\Delta\Delta\text{Ct})$  method. *Methods* **2001**, *25* (4), 402–408.
- (27) Ivey, K. N.; Muth, A.; Arnold, J.; King, F. W.; Yeh, R. F.; Fish, J. E.; Hsiao, E. C.; Schwartz, R. J.; Conklin, B. R.; Bernstein, H. S.; Srivastava, D. MicroRNA regulation of cell lineages in mouse and human embryonic stem cells. *Cell Stem Cell* **2008**, *2* (3), 219–229.
- (28) Bi, Y. M.; Stuelten, C. H.; Kilts, T.; Wadhwa, S.; Iozzo, R. V.; Robey, P. G.; Chen, X. D.; Young, M. F. Extracellular matrix proteoglycans control the fate of bone marrow stromal cells. *J. Biol. Chem.* **2005**, *280* (34), 30481–30489.
- (29) Yang, M.; He, W.; Shuai, Y.; Min, S.; Zhu, L. Nucleation of hydroxyapatite crystals by self-assembled *Bombyx mori* silk fibroin. *J. Polym. Sci.* **2013**, *51* (9), 742–748.
- (30) Li, Z.; Lam, W.; Yang, C.; Xu, B.; Ni, G.; Abbah, S.; Cheung, K.; Luk, K.; Lu, W. Chemical composition, crystal size, and lattice structural changes after incorporation of strontium into biomimetic apatite. *Biomaterials* **2007**, *28* (7), 1452–1460.
- (31) Cai, Y.; Jin, J.; Mei, D.; Xia, N.; Yao, J. Effect of silk sericin on assembly of hydroxyapatite nanocrystals into enamel prism-like structure. *J. Mater. Chem.* **2009**, *19* (32), 5751.
- (32) Khire, T. S.; Kundu, J.; Kundu, S. C.; Yadavalli, V. K. The fractal self-assembly of the silk protein sericin. *Soft Matter* **2010**, *6* (9), 2066–2071.
- (33) Russel, W. Brownian motion of small particles suspended in liquids. *Ann. Rev. Fluid Mech.* **1981**, *13* (1), 425–455.
- (34) Ruoslahti, E.; Pierschbacher, M. D. New perspectives in cell adhesion: RGD and integrins. *Science* **1987**, *238* (4826), 491–497.
- (35) Wang, J.; Wang, L.; Li, X.; Mao, C. B. Virus activated artificial ECM induces the osteogenic differentiation of mesenchymal stem cells without osteogenic supplements. *Sci. Rep.* **2013**, *3*, 1242.
- (36) Zhu, H.; Cao, B.; Zhen, Z.; Laxmi, A.; Li, D.; Liu, S.; Mao, C. B. Controlled growth and differentiation of mesenchymal stem cells on grooved films assembled from monodisperse biological nanofibers with genetically tunable surface chemistries. *Biomaterials* **2011**, *32*, 4744–4752.
- (37) Chou, Y. F.; Dunn, J. C.; Wu, B. M. In vitro response of MC3T3 E1 preosteoblasts within three-dimensional apatite-coated PLGA scaffolds. *J. Biomed. Mater. Res.* **2005**, *B75* (1), 81–90.

(38) Bourgeois, B.; Laboux, O.; Obadia, L.; Gauthier, O.; Betti, E.; Aguado, E.; Daculsi, G.; Bouler, J. M. Calcium-deficient apatite: A first *in vivo* study concerning bone ingrowth. *J. Biomed. Mater. Res.* **2003**, A65 (3), 402–408.

(39) Rosa, A. L.; Beloti, M. M.; Van Noort, R.; Hatton, P. V.; Devlin, A. J. Surface topography of hydroxyapatite affects ROS17/2.8 cells response. *Pesqui. Odontol. Bras.* **2002**, 16 (3), 209–215.